Rejuvenation-deformation relationship of a well-aged metallic glass during Newtonian to non-Newtonian flow

Y. Gao [a,b], G. Ding [a], C. Yang [a,b], B.B. Zhang [c], C.J. Shi [c], L.H. Dai [a,b], M.Q. Jiang [a,b,*]

[a] *State Key Laboratory of Nonlinear Mechanics, Institute of Mechanics, Chinese Academy of Sciences, Beijing 100190, PR China*
[b] *School of Engineering Science, University of Chinese Academy of Sciences, Beijing 100049, PR China*
[c] *Institute of High Energy Physics, Chinese Academy of Sciences, Beijing 100049, PR China*

ARTICLE INFO

ABSTRACT

Stress overshoot is a sign of structural rejuvenation of metallic glass, which usually occurs in non-Newtonian flow with large strain rate. Here we show a heavily-aged Zr-based metallic glass that rejuvenates by low-strain-rate Newtonian flow without showing any stress overshoot. Its rejuvenation does not increase the energy level of its basin of potential energy landscape, but reduces the basin's mechanical stability. Synchrotron X-ray total scattering gives direct evidence that under Newtonian flow, the rejuvenation is contributed by complex structural rearrangements over short- and medium-range order scales. We further find that due to the structurally inhomogeneous response, there is an optimal strain rate for rejuvenation, above which the energy level decreases, but the characteristic size of the medium-range order continues to increase. Thus, the mechanical stability and structural disorder do not decrease synchronously. Our findings refresh the understanding of the relationship between mechanical deformation and structural rejuvenation in metallic glasses.

1. Introduction

Thermo-mechanical deformation is an excellent strategy to regulate the energy level and local atomic configurations of metallic glasses (MGs). Under thermo-mechanical deformation, the physical aging of MGs possibly occurs as they evolve to lower energy states with local order. On the other hand, thermo-mechanical deformation has been widely used to rejuvenate aged or as-quenched glasses to higher energy states with complex atomic configurations [1,2]. And there is a threshold for rejuvenation that only occurs when sufficient external energy is injected [3,4]. Therefore, it is very important to reveal the relationship between thermo- mechanical deformation and aging/rejuvenation in MGs [5,6].

With increasing strain rate, the thermo-mechanical homogeneous deformation of MGs can show the mode transition from Newtonian to non-Newtonian flow [7,8]. At lower strain rates, the steady-state flow stress σ_f is linearly related to the strain rate $\dot\varepsilon$, which means that the steady-state viscosity ($\eta = \sigma_f/3\dot\varepsilon$ [9]) remains constant at a given temperature, and the deformation is in the Newtonian regime. At this point, internal structural relaxation is fast enough to keep up with the external loading, resulting in a monotonically increasing strain-strain curve.

Above a critical strain rate, the linear $\sigma_f - \dot\varepsilon$ relationship is broken with a non-constant η, and the flow is in the non-Newtonian regime. In this situation, the external loading is too fast for the internal structure relaxation to match, so the stress-strain curves exhibit the stress overshoot before the steady-state flow. Whether in experiments [10], simulations [11] or theoretical analyses [12], the stress overshoot is accompanied by the increase of free volume of MGs, that is, the energy level increases and the structural rejuvenation. Ding et al. [13] define the area of stress overshoot as the effective energy density, which can be used to measure the degree of structural rejuvenation. The stress overshoot increases with the increase of strain rate, and so does the degree of rejuvenation [14,15]. It seems clear that for the rejuvenation by increased level, the transition from aging to rejuvenation corresponds to the transition from Newtonian to non-Newtonian flow. However, our previous study [16] found that for well-aged MGs, rejuvenation is not necessarily an increase in energy level, but can be achieved by reducing the mechanical stability of its basin of potential energy landscape (PEL). Both rejuvenation and deformation are strongly dependent on their initial structure. The influence of the initial structure of well-aging on rejuvenation has been reported by Zhou et al. [17]. They found that there was still a gap between the vibrational dynamics of the as-cast and

---

the well-aged samples, after rejuvenated to approximately similar energy levels by high-pressure torsion severe deformation. The appearance of this gap is inferred to be strongly related to the initial tremendous difference of the mechanical stability between the two sets of samples. This indicates that thermal history residue will affect the structural rejuvenation after sufficient relaxation into a fairly deep basin. It has also been shown that thermal history can be erased by stress overshoot and anelastic deformation when relaxation is not sufficient, and that the eventual steady-state condition is independent of them [18]. Then, the relationship between steady-state flow deformation and rejuvenation of fully relaxed MGs urgently needs in-depth studies.

In this work, to decouple the two mechanisms of mechanical stability decrease and energy level increase, we specially prepare a heavily-aged Zr-based MG whose initial state has almost no free volume. Uniaxial compression at 663 K is performed on this very stable glass at different strain rates, and a transition from Newtonian to non-Newtonian flow is obtained. Here we use calorimetric enthalpy, low-temperature heat capacity boson peak and X-ray total scattering to analyze the strain rate evolution of the structural rejuvenation. The results show that the thermal history of the initial structure traps the MG in a deep enough basin, where further aging and free volume generation are inhibited. In Newtonian flow regime, the reduction of mechanical stability induced by structural rearrangement plays an important role in the rejuvenation. In non-Newtonian flow regime, rejuvenation is dominated by a net increase in free volume. Furthermore, we find that the trend of increasing rejuvenation with the acceleration of strain rate stops before local deformation, or even the opposite trend appears, which is also closely related to the structural rearrangement at the MRO scale.

2. Materials and methods

$Zr_{52.5}Cu_{17.9}Ni_{14.6}Al_{10}Ti_5$ MGs possess an excellent glass-forming ability and relatively high thermal stability, so it is an ideal model for studying mechanical rejuvenation. Alloy ingots were prepared by arc melting the mixtures of pure constituents ($> 99.99\%$) under the protection of high-purity argon atmosphere. Each ingot was arc-melted in a vacuum arc furnace four times to ensure chemical homogeneity. Robs with a diameter of 5 mm were prepared by copper mold suck casting. Cylindrical samples with a length of 8 mm were cut from the as-cast rods, and then carefully ground to ensure that the two ends are parallel. All samples were vacuum-annealed for 12 h at 643 K to completely release the excess free volume. The amorphous structures of the pre-annealed glasses were verified by X-ray diffraction (XRD, Rigaku Smart Lab 9) with Cu Kα radiation. Calorimetric measurements were performed by differential scanning calorimetry (DSC, TA DSC25) with a heating rate of 20 K/min under a pure argon atmosphere. Samples were heated from room temperature to 773 K and held for 2 min, then cooled to room temperature at 10 K/min. Use the same procedure for a second cycle to obtain a baseline. According to the measured DSC curves, the onset of the glass transition temperature T_g and the onset of the crystallization temperature T_x for the pre-annealed samples were about 673 K and 703 K, respectively. The excess exothermic enthalpy ΔH prior to the glass transition evaluated the energy level of the glass basin in PEL. The enthalpy changes during the glass-to-liquid transition were calculated as the effective enthalpy ΔH_{eff} to evaluate the degree of configurational disorder, as described in more detail in our previous work [16]. The pre-annealed samples show almost no ΔH, and a sufficiently small ΔH_{eff} with a very pronounced glass transition "overshoot''. That is, we successfully obtained a batch of very stable, well-aged glasses.

The thermo-mechanical compression tests were performed on the well-aged glasses with a microcomputer controlled universal testing machine at 663 K. The shear component in uniaxial compression significantly reduces the T_g [19], and the deformation is easy to enter the supercooled region at the current loading temperature. Therefore, samples can undergo homogeneous liquidlike inelastic deformation rather than localized deformation within a certain strain rate range. The

strain rates were chosen as: $2 \times 10^{-5}\ s^{-1}$, $4 \times 10^{-5}\ s^{-1}$, $5 \times 10^{-5}\ s^{-1}$, $6 \times 10^{-5}\ s^{-1}$, $2 \times 10^{-4}\ s^{-1}$, $4 \times 10^{-4}\ s^{-1}$, $6 \times 10^{-4}\ s^{-1}$, $8 \times 10^{-4}\ s^{-1}$, and $1 \times 10^{-3}\ s^{-1}$. Before loading, the furnace was preheated to 663 K for an hour to reach a stable state. Samples were rapidly placed into the furnace and held for 10 min to attain thermal equilibrium. At each strain rate, samples were compressed to an engineering strain of 0.2, at which point the deformation has entered a steady-flow state. Recently, many studies have pointed out that at a given temperature and strain rate, the system is already in dynamic equilibrium at steady state [6,20]. After compressions, the samples were immediately quenched into iced water to capture the instantaneous configuration as much as possible. The fully amorphous nature of all deformed samples was evidenced by XRD.

In the middle of the cylindrical samples, perpendicular to the loading direction, thin slices were cut from each deformed sample and then carefully polished for subsequent rejuvenation characterization. The exothermic enthalpy ΔH and the effective enthalpy ΔH_{eff} were measured by DSC at high-temperature ($450\ K \leq T \leq 770\ K$). The vibrational dynamics of MGs can also reflect the degree of structural rejuvenation. At terahertz frequencies, MGs usually display an excess of vibrational modes over the Debye level, forming the boson peak (BP) [21]. It can be measured using a Quantum Design physical property measurement system (PPMS) at low-temperature ($1.9\ K \leq T \leq 100\ K$). Stronger BPs with lower frequencies usually correspond to heavier rejuvenation [22], reflecting an increase in the curvature at the bottom of the basins and a decrease in mechanical stability. To further analyze the structural information, synchrotron X-ray total scattering experiments were carried out at beamline 3W1 of Beijing Synchrotron Radiation Facility (BSRF), using an incident X-ray beam of wavelength 0.2085655 Å (59.45 keV). A large-area detector (Mercu 1717HS, 3072×3048 pixels of 139 um × 139 um CsI) was placed ~180 mm downstream of the sample, giving a Q_{max} of 24 Å^{-1}. The setup was calibrated using the diffraction pattern from polycrystalline CeO_2 powder. Sample was attached to the aluminum alloy frame with Compton tape. The measurement procedure was controlled by Idetector software and the exposure time 5 s was set for all of the samples. Background patterns were collected with the same setup and exposure time. The raw diffraction data was deduced from two-dimensional images, the effects of polarization and geometry were corrected using the Fit2D program [23]. Absorption, geometry, detector effects, and the normalization procedure were carried out using PDFgetX2 [24].

3. Results and discussion

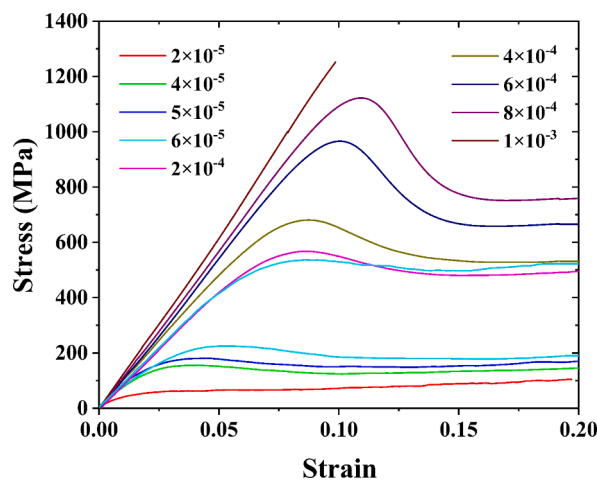In Fig. 1, we present the compressive stress-strain responses of

Fig. 1. Stress–strain curves for samples deformed with different strain rates at 663 K. From these curves the flow stress σ_f is obtained for each strain rate and viscosity is calculated by using the equation: $\eta = \sigma_f/3\dot{\varepsilon}$.

samples deformed at increasing strain rates. At low strain rates $\dot{\varepsilon} < 6 \times 10^{-5}$ s^{-1}, the stress increases monotonically with strain and eventually attains a steady-state flow stress σ_f. At high strain rates $\dot{\varepsilon} > 6 \times 10^{-5}$ s^{-1}, the stress increases initially attaining a maximum value and then decreases to a steady-state value. The stress overshoot is attributed to the creation of free volume or the formation of rheological defects, and is closely correlated to structural rejuvenation [25]. At a higher strain rate $\dot{\varepsilon} = 1 \times 10^{-3}$ s^{-1}, the stress increases almost linearly with the strain, and the localized deformation occurs suddenly when the stress is near the peak. At the experimental critical strain rate $\dot{\varepsilon} = 6 \times 10^{-5}$ s^{-1}, the stress-strain response is very sensitive. As shown by the two blue curves in Fig. 1, there is a large gap between them, with one close to the Newtonian flow response and the other close to the non-Newtonian flow response.

The strain rate dependence of viscosity is displayed in Fig. 2(a). The steady-state flow viscosity at a given temperature remains constant at low strain rates and decreases above a critical strain rate, indicating the Newtonian to non-Newtonian flow transition with increasing strain rate. At the current experimental temperature, the Newtonian viscosity is about 1.5×10^{12} Pa s, which is close to the viscosity ($\eta_g \sim 10^{12}$ Pas $\eta_g \sim 10^{12}$ Pa s) at the T_g [26]. And the non-Newtonian viscosity is lower than the η_g, indicating that the deformation has entered the supercooled region, as preset previously. The critical strain rate of the transition from Newtonian to non-Newtonian flow is in the interval of 6×10^{-5} s^{-1}~2×10^{-4} s^{-1}, corresponding to the critical strain rate of the stress overshoot. Fig. 2(b) shows normalized viscosity η

$/\eta_N$ as a function of shear time t. The shear time is the inverse of the shear rate $\dot{\gamma} = \sqrt{3}\dot{\varepsilon}$, where $\dot{\varepsilon}$ is the compressive strain rate. The η/η_N vs. shearing time is well fitted by a simple exponential response function: $\frac{\eta}{\eta_N} = 1 - \exp\left(-\frac{t}{\tau}\right)$, with relaxation time $\tau = 3838$ s $\pm$ 638 s, as shown by the red line. Thus, the relaxation rate at 663 K is $(2.68 \pm 0.45) \times 10^{-4}$ s^{-1}, which is exactly between shear rates 1.04×10^{-4} s^{-1} and 3.46×10^{-4} s^{-1} corresponding to strain rates 6×10^{-5} s^{-1} and 2×10^{-4} s^{-1}. This result is consistent with that observed in the experiments. It indicates that the observed critical behaviors are the result of shear rate beginning to be faster than the structural relaxation rate, which is the mechanism of rejuvenation caused by the increase of free volume. The rejuvenation behavior behind the deformation is discussed below.

Figure 3 presents the specific heat capacity C_p curves obtained from DSC for well-aged and deformed samples in Fig. 1(a). For visual comparison, all curves are subtracted from the baseline data from the second heating. The dashed lines shown in Fig. 3 are the horizontal extension of the pre-exothermic C_p curves as the new baselines. The exothermic area enclosed below the baseline in the DSC curve is equal to ΔH, and ΔH minus the endothermic area enclosed above the baseline is equal to ΔH_{eff}. The well-aged samples show no exothermic area, and even the DSC curve is above the baseline. In the Newtonian regime ($\dot{\varepsilon} \leq 6 \times 10^{-5}$ s^{-1}), the exothermic areas are extremely weak, without a significant change. This trend is consistent with the deformation process, that the time scale of internal structural relaxation is comparable to the external loading rate. Newtonian flow does not introduce excess free volume into the system. As reported previously [27–29], at low strain rates, thermally activated internal structural relaxation governs the plastic flow, which can even reduce the free volume and age the MG. But this relaxation is inhibited by the heavily-aged initial structure. In the non-Newtonian regime ($\dot{\varepsilon} > 6 \times 10^{-5}$ s^{-1}), the exothermic areas gradually increase and the distribution gradually broadens. The enhancement of exothermic implies an increase in defect concentration based on the quasi-point defects (QPD) theory [30], which means that the flow translating to stress dominated. This result is consistent with the observed stress overshoot in deformation. It can also be seen that the exothermic area does not monotonically increase with the strain rate. As the strain rate continues to increase until the deformation localization, the exothermic area reversely decreases. This peak effect of rejuvenation, which is affected by strain rate, was also observed by Tong et al. [31] who suggested it may be related to strain localization before the inhomogeneous plastic deformation. However, in our experiments, at such high strain rates, the deformations still enter a steady-flow state, and the viscosities are smaller than that at T_g. This indicates that the deformation has entered the supercooled region and is homogeneous.

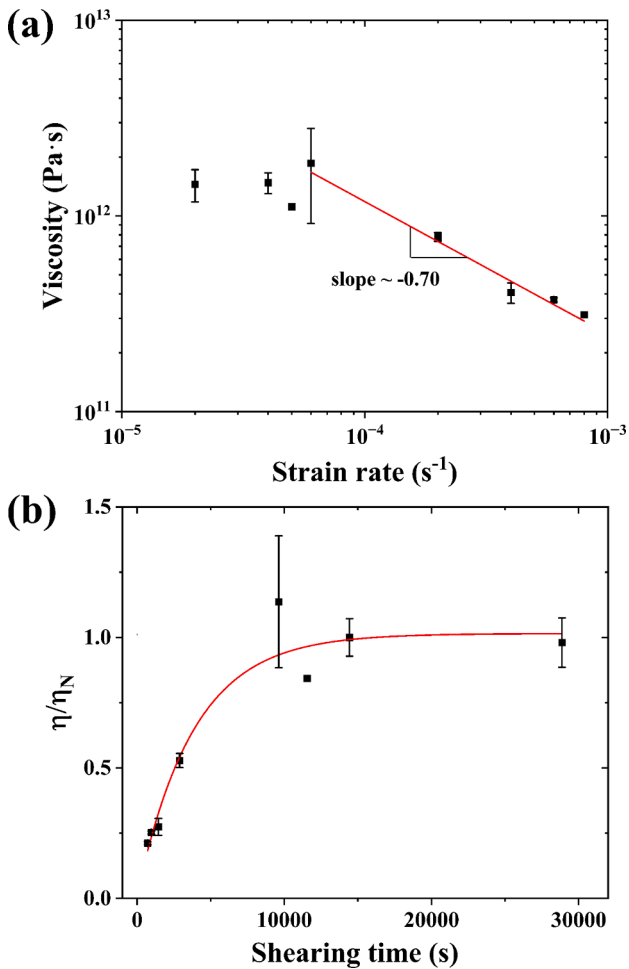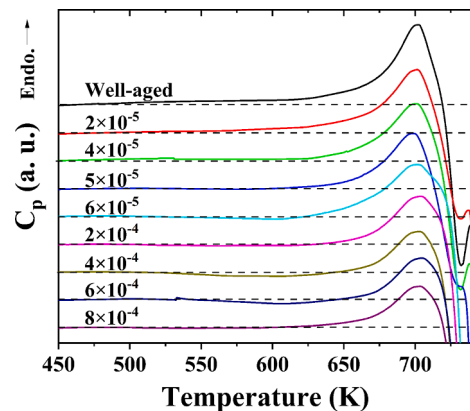According to the measured DSC curves, the variation of the

Fig. 2. (a) Viscosity–strain-rate relationship. Here the transition from Newtonian to non-Newtonian flow is observed. (b) Normalized viscosity, η/η_N, as a function of the shearing time at 663 K. The red line is the fitting curve.

Fig. 3. The specific heat capacity curves of samples for well-aged and deformed at different strain rates: 2×10^{-5} s^{-1}, 4×10^{-5} s^{-1}, 5×10^{-5} s^{-1}, 6×10^{-5} s^{-1}, 2×10^{-4} s^{-1}, 4×10^{-4} s^{-1}, 6×10^{-4} s^{-1}, and 8×10^{-4} s^{-1}.

endothermic area is also observed. In the framework of the soft-hard model [32], deep annealing at high-temperature can sharply shrink the average inter-atomic distance in the soft region. Simultaneously, the activation energy of partial soft region is raised to the level of hard region, resulting in a very obvious glass transition "overshoot'' [33], as shown by the black line in Fig. 3, and the heat capacity curve of the well-aged sample is always above the baseline. In Newtonian flow regime, the endothermal areas of glass transition "overshoot" become more depressed and narrower monotonically. The decrease of the high "overshoot" of the well-aged glass can be reasoned as the gradual recovery of soft region with high activation energy by Newtonian flow, that is, the reduction of the higher number density of hard regions, which indicates that the glassy structure is more unstable. After non-Newtonian flow, most of the densified soft regions have been restored, and the expansion of the hard region is limited by the non-homogeneous deformation, so this depressed rate is obviously slowed down. This interesting phenomenon is discussed in detail below in conjunction with structural information.

The low-temperature C_p between 1.9 K and 100 K of the well-aged and deformed glasses was measured. The total low-temperature C_p contains the phonon and electronic contributions, which is given as: $C_p = C_{ph} + C_{el} = \beta T^3 + \gamma T$. As indicated above, the BP is a low-frequency enhancement of the vibrational density of states (VDOS) in the C_{ph} as compared to the Debye T^3 law. In order to subtract the electronic contribution, C_p is plotted vs T^2 below 8 K to fit the values of the Sommerfeld coefficient γ [34]. The BPs are then easily visualized in the plot
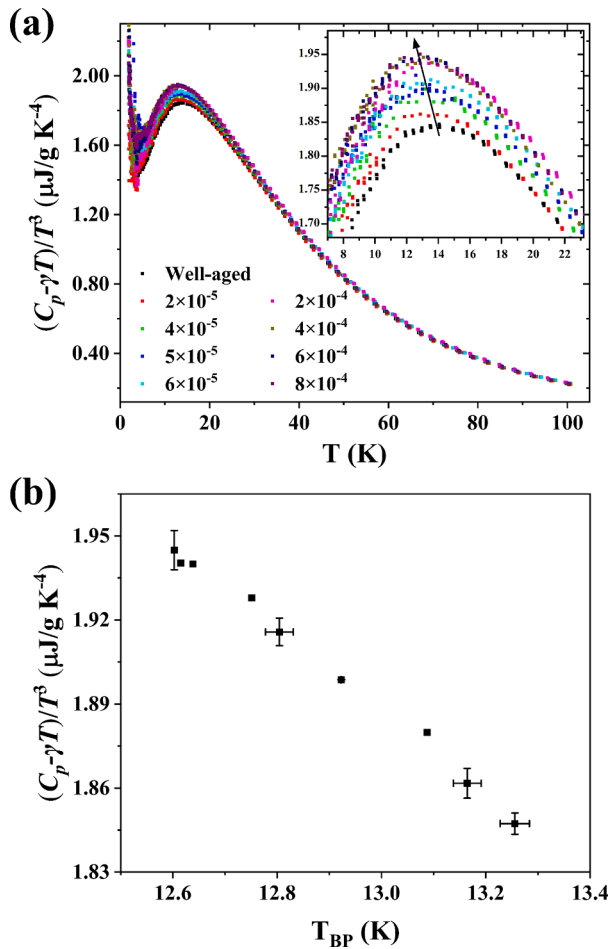
of $(C_p - \gamma T)/T^3$ vs T, as shown in Fig. 4(a). The BPs appear as maxima between 12 and 16 K, which are highlighted in the inset of Fig. 4(a). We can see that the well-aged sample shows the weakest BP and the highest peak temperature. In the Newtonian regime, with the increase of strain rate, BP becomes stronger and more pronounced, and the peak maximum shifts to lower T. As a manifestation of heterogeneous distribution of local disorder, this increase in BP can reasonably be considered as rearrangement induced structural rejuvenation. In the non-Newtonian regime, the BP evolution does not increase monotonically with strain rate, and no longer increases when the strain rate is greater than $4 \times 10^{-4} \ s^{-1}$. The initial increase corresponds to an enhancement of the exothermic area in DSC and can be attributed to a net increase in free volume. Later, the BP saturation at higher strain rates results from complex structural changes. The relationship between the BP height and temperature is shown in Fig. 4(b). This linear relationship for all samples, including well-aged and deformation at different strain rates, is in agreement with the previous results [34].

For a more intuitive comparison, the quantitative changes of excess enthalpy ΔH, normalized effective enthalpy $\Delta H_{eff}/\Delta H_{eff-ann}$ and inverse BP temperature $1/T_{BP}$ with strain rate are shown in Fig. 5. The red horizontal dashed line denotes the corresponding value of the well-aged sample. The ordinate in Fig. 5(b) is normalized by the effective enthalpy of the pre-annealed well-aged sample, $\Delta H_{eff-ann}$. Here is an intriguing phenomenon, in Newtonian flow regime, the evolution of ΔH with strain rates is different from $\Delta H_{eff}/\Delta H_{eff-ann}$ and $1/T_{BP}$. The ΔH shows almost no change with low strain rates (Fig. 5(a)), indicating that Newtonian flow is insufficient to introduce free volume into this stable glass. The value of ΔH of the well-aged sample is 0.07 J/g, so it does not exhibit a decrease in ΔH as mentioned in other works [35]. These results are attributed to pre-annealing trapping the MG in a deep enough basin, thereby inhibiting further aging and free volume generation. As shown in Fig. 5(b) and (c), $\Delta H_{eff}/\Delta H_{eff-ann}$ and $1/T_{BP}$ even increase monotonically with low strain rates. The former includes the influence of excess enthalpy and glass transition "overshoot". Given that there is no
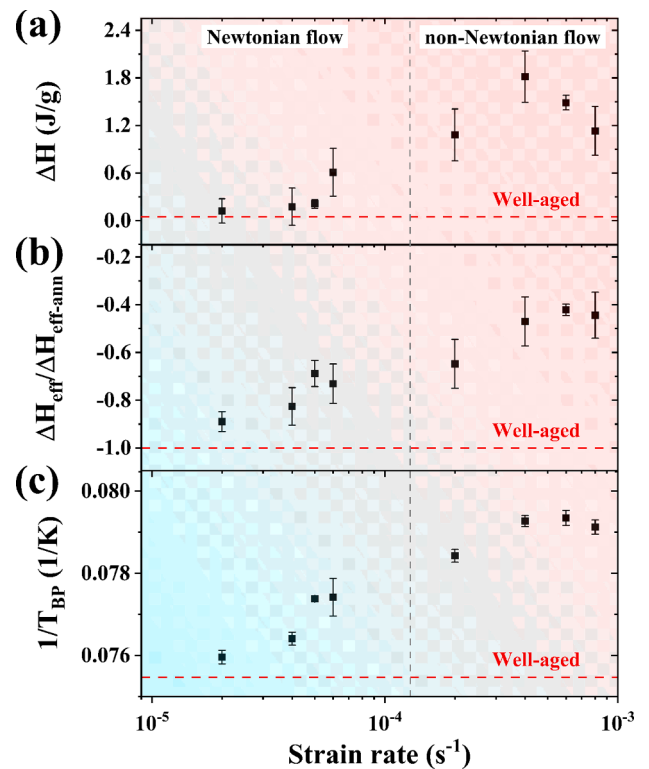

Fig. 4. (a) Low-temperature boson heat capacity peaks of samples for well-aged and deformed at different strain rates. The boson peak is highlighted in the inset. (b) Linear correlation between the boson peak heights and the peak positions.

Fig. 5. (a) Excess enthalpy ΔH, (b) normalized effective enthalpy $\Delta H_{eff}/\Delta H_{eff-ann}$ and (c) inverse BP temperature as a function of the strain rate.

visible change in ΔH, the increase in $\Delta H_{\mathrm{eff}}/\Delta H_{\mathrm{eff-ann}}$ is contributed by the decrease in glass transition "overshoot". It indicates that with the increase of strain rate, structural rearrangement intensifies the configuration disorder of MGs. The latter can reflect structural vibration information across scales, including atomic-scale free volume and nanoscale cluster rearrangements [36,37]. As previously discussed [17], atoms located at a more loose area vibrate stronger and contribute more to the excess VDOS, with BP occurring at a relatively low temperature. From the PEL viewpoint, the increase of $1/T_{BP}$ is linked with the shallowness of the basin and the decrease of the activation barrier [38]. This supports that Newtonian flow reduces the mechanical stability of this stable glass. The greater instability and disorder point to rejuvenation, even if the energy level of the glass remains almost unchanged. The difference in the evolution of ΔH and $1/T_{BP}$ with low strain rates once again emphasizes the importance of structural rearrangement in glass rejuvenation.

In non-Newtonian flow regime, the ΔH evolves in two stages with strain rate, as do $\Delta H_{\mathrm{eff}}/\Delta H_{\mathrm{eff-ann}}$ and $1/T_{BP}$. In the first stage ($6 \times 10^{-5}\ s^{-1} \leq \dot{\varepsilon} \leq 4 \times 10^{-4}\ s^{-1}$), they all increase monotonically with strain rate. It can be explained that at high strain rates, slow internal structural relaxation processes are significantly limited by short timescales, with external loads prevailing. Non-Newtonian flows activate sufficient shear transformations (STs) to introduce free volume into this stable glass. This process is accompanied by an increase in the size and/or the number of the soft regions, in which STs are inclined to initiate. Resulting in reduced mechanical stability and enhanced structural disorder. These evolutions are consistent with the previous rejuvenation works [39,40]. In the second stage ($4 \times 10^{-4}\ s^{-1} \leq \dot{\varepsilon} \leq 8 \times 10^{-4}\ s^{-1}$), it can be seen in Fig. 5(a) that ΔH decreases with the increase of strain rate. A significant decrease from about 1.81 J/g to about 1.13 J/g in ΔH means a reduction in the free volumes introduced into the MG, and a downward energy level. Such reduction is largely offset by glass transition "overshoot", so $\Delta H_{\mathrm{eff}}/\Delta H_{\mathrm{eff-ann}}$ remains stable at excessively high strain rates, as indicated in Fig. 5(b). It shows that under the combined influence of free volume and structural distribution, the structural disorder of MG does not change significantly. The atomic vibrations are also influenced by free volume and structural distribution [41]. In Fig. 5 (c), the $1/T_{BP}$ also stabilizes with excessive strain rates, which implies mechanical stability is saturated and rejuvenation has reached its limit. The asynchronicity of energy level, configuration disorder, and mechanical stability is observed again. We speculate that this is due to the excess strain rate further increasing the size of the soft regions while expanding the hard regions, during the stress overshoot deformation stage. In the plastic deformation, the large amount of free volume in the soft region in turn accelerates its own annihilation. Moreover, in this limiting rejuvenation state, the expanded hard regions lead to a decrease in the free volume that the system can accommodate. These two factors together lead to a decrease in ΔH. Eventually, the disorder brought about by the expansion of the hard regions and the order caused by the annihilation of the free volume cancel each other out. The decrease in the degree of rejuvenation caused by this excess energy injection was also obtained by Gong et al. [42].

In the following, we address the topologically structural information of the MG rejuvenation. The 2-D diffraction patterns of well-aged and deformed samples obtained by X-ray total scattering show typical amorphous diffraction halos. The azimuth integral of the diffraction halos can obtain the raw intensity curve, which is normalized by the intensity of the first peak after correction, and the normalized intensity curves $I(Q)$ are shown in Fig. 6(a). Increasing the strain rate does not significantly change the structure of the glass. Detailed view of the first peak in the fitted $I(Q)$ curves at different strain rates reveals that the peak position Q slightly changes with increasing strain rate (see the inset in Fig. 6(a)). The first scattering peak Q contains structural information of the MRO in the glassy phase, which is also affected by short-range order (SRO) [43,44]. The quantitative change of the normalized first
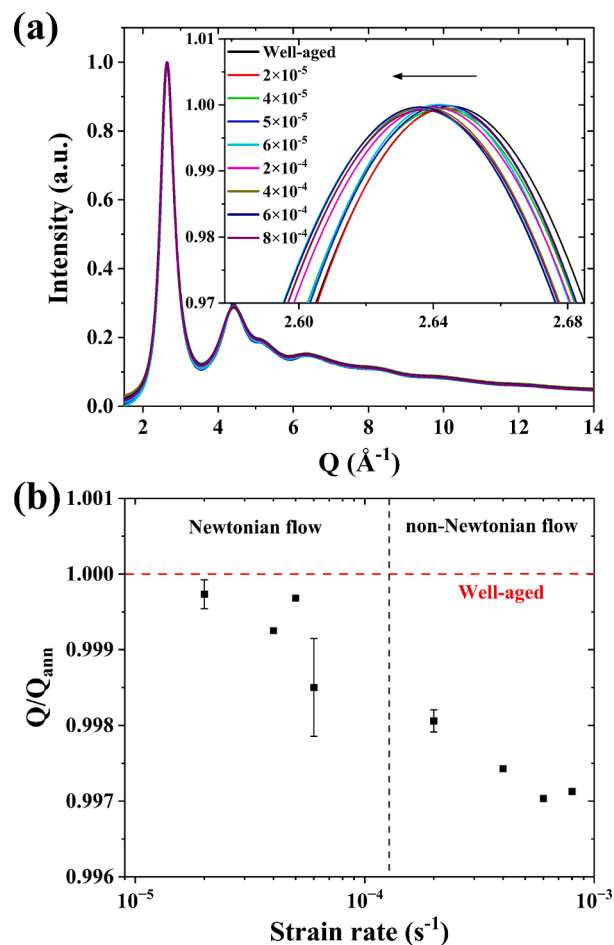

Fig. 6. (a) X-ray scattered intensity curves of samples for well-aged and deformed at different strain rates. Inset highlights the positions of the first peaks. (b) Change of the normalized position values of the first maximum Q/Q_{ann} with the strain rate.

peak position Q/Q_{ann} with strain rate is given in Fig. 6(b), where Q_{ann} is the first peak position of the well-aged sample. In Newtonian flow regime, Q/Q_{ann} shifts to a lower value with the increase of strain rate, corresponding to an expansion in the interatomic distance with increasing strain rate. It is consistent with the results following from the ΔH_{eff} and BP in Figs. 3 and 4, all of which are related to MRO. But it differs from the evolution of ΔH with strain rate, and ΔH is more sensitive to SRO. This suggests that the structural changes are inhomogeneous with increasing strain rate. In non-Newtonian flow regime, Q/Q_{ann} first continued to decrease and then stabilized. Combined with the calorimetric enthalpy and vibrational results above, the further expansion of interatomic distance in the first stage is contributed by the increase of atomic-scale free volume and the rearrangement of nanoscale clusters. At large strain rates close to failure, the invariance of interatomic distance does not match the decrease in ΔH. This suggests that the structural changes occur in different atomic shells, that is, they are inhomogeneous.

To further characterize the different changes in different shells, the pair distribution functions ($G(r)$) in real space are investigated (Fig. 7). $G(r)$ is obtained by taking the Fourier transform of the scattered intensity curves in Fig. 6(a). Considering that the strain rate does not significantly change the glass structure at the current strain rate span, four typical strain rates in Fig. 1 are selected for structural analysis: $2 \times 10^{-5}\ s^{-1}, 5 \times 10^{-5}\ s^{-1}, 4 \times 10^{-4}\ s^{-1}$ and $8 \times 10^{-4}\ s^{-1}$. The first peak of the $G(r)$ in the range of $2 \sim 4$ Å, representing the SRO of the MGs. Fig. 7 (b) gives a detailed view of the first peak, showing that it splits into two
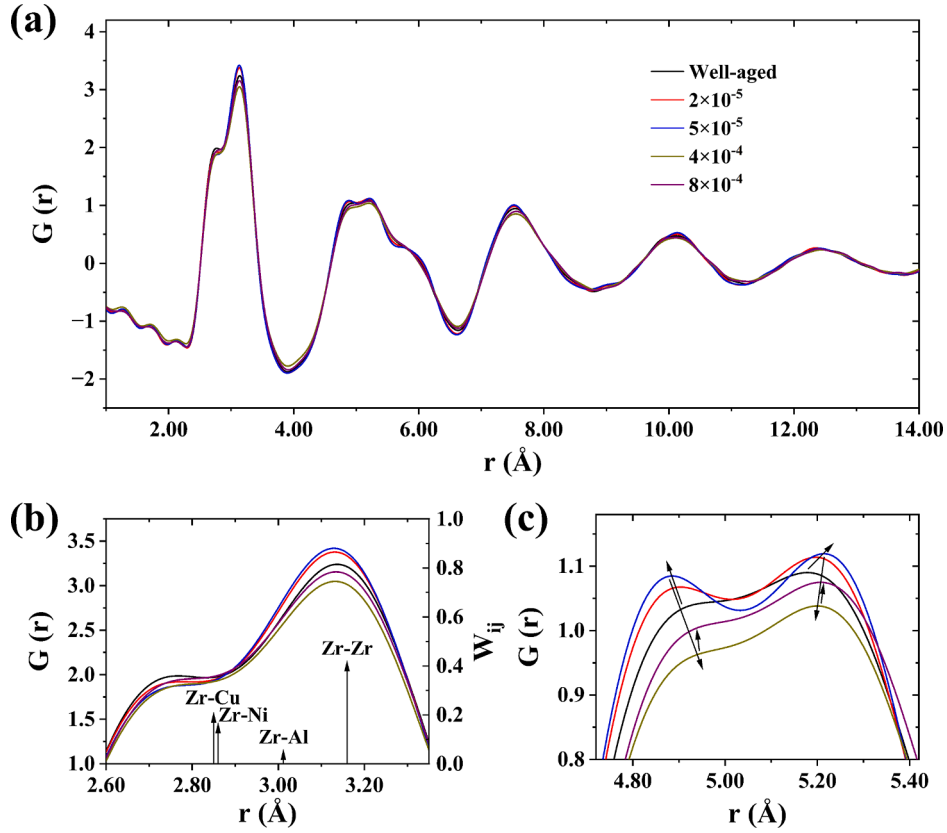
Fig. 7. Pair distribution functions (PDFs) analysis of well-aged sample and deformed samples inferred from X-ray scattered. (a) Overall trend of PDF curves. Detailed view of the first peak and (c) the second peak.

sub-peaks due to the discrete bond length distribution of the nearest neighbor atoms. In order to determine the dominant bonds at SRO scale, it is required to consider the interatomic bond length, probability factor ($P_{ij} = \delta c_i c_j$) [45], and the corresponding weight factors W_{ij}. W_{ij} is calculated in the following manner [46,47]:

$$
W_{ij} = \begin{cases} \dfrac{2c_i c_j f_i(Q) f_j(Q)}{\left[\displaystyle\sum_{k=1}^{n} c_k f_k(Q) \right]^2}, i \neq j \\[4ex] \dfrac{c_i^2 f_i^2(Q)}{\left[\displaystyle\sum_{k=1}^{n} c_k f_k(Q) \right]^2}, i = j \end{cases} \tag{1}
$$

where c is the atomic concentration of elements; $f(Q)$ is the scattering factor of the atomic species; i and j represent different elements. The W_{ij} is calculated at $Q = 0$ Å^{-1}, where $f(0)$ is the atomic fraction of the element. These calculations are explicitly listed in Table 1.

From the type and concentration of the constituent elements in the $Zr_{52.5}Cu_{17.9}Ni_{14.6}Al_{10}Ti_5$, it is clear that Zr-Zr, Zr-Cu, Zr-Ni and Zr-Al are the dominant atomic pairs which constitute the SRO of the PDFs. Their interatomic bond lengths and the corresponding weight factors are also plotted in Fig. 7(b). The first sub-peak mostly belongs to the Zr-Cu and Zr-Ni atomic pairs, while the second sub-peak at longer distance can be sign of Zr-Al and Zr-Zr atomic pairs. Fig. 8(a) shows the result of the deconvolution for the SRO of samples in Fig. 7. The center of the first peak is about 2.69 Å, corresponding to the Zr-(Cu, Ni) atomic pairs. The second peak centered about 3.14 Å originates from Zr-(Zr, Al) atomic pairs. The enlarged first peak and second peak are shown in Fig. 8(b) and (c), respectively. In Newtonian flow regime ($\dot{\varepsilon} = 2 \times 10^{-5}$ s^{-1}, 5×10^{-5} s^{-1}), an increase in strain rate shifts the first peak to the lower left and the second peak to the upper left. The unexpected change in the

Table 1
Inter-atomic bond lengths and weight factors of atomic pairs in the $Zr_{52.5}Cu_{17.9}Ni_{14.6}Al_{10}Ti_5$, metallic glass.

Bond type	Bond length (Å)	Weight factor	Probability factor
Zr-Zr	3.16	0.413	0.276
Zr-Cu	2.85	0.204	0.188
Zr-Ni	2.86	0.161	0.153
Zr-Al	3.01	0.051	0.105
Zr-Ti	3.03	0.043	0.053
Cu-Cu	2.54	0.025	0.032
Cu-Ni	2.55	0.040	0.052
Cu-Al	2.70	0.013	0.036
Cu-Ti	2.72	0.011	0.018
Ni-Ni	2.56	0.016	0.021
Ni-Al	2.71	0.010	0.029
Ni-Ti	2.73	0.008	0.015
Al-Al	2.86	0.002	0.010
Al-Ti	2.88	0.003	0.010
Ti-Ti	2.9	0.001	0.003

position of the two peaks suggests that Newtonian flow causes the contraction in SRO. Considering the height of the peaks, it does not exhibit an overall decrease in height as typical rejuvenation, but shows a decrease in the first peak while an increase in the second peak. This indicates that the formation of Zr-(Zr, Al) atomic pairs may be accompanied by the annihilation of Zr-(Cu, Ni) atomic pairs in the microstructure of the MGs. These structural rearrangements of bonding switches on the atomic scale are also detected in Refs. [48–50]. As Zhao calculated [51], a long atomic pair is related to a high cluster energy. The bond switch from tight Zr-(Cu, Ni) atomic pairs to long Zr-(Zr, Al) atomic pairs enhances the potential energy, but this enhancement may be offset by the contraction of the SRO. This precisely explains the phenomenon that the ΔH does not change significantly with increasing
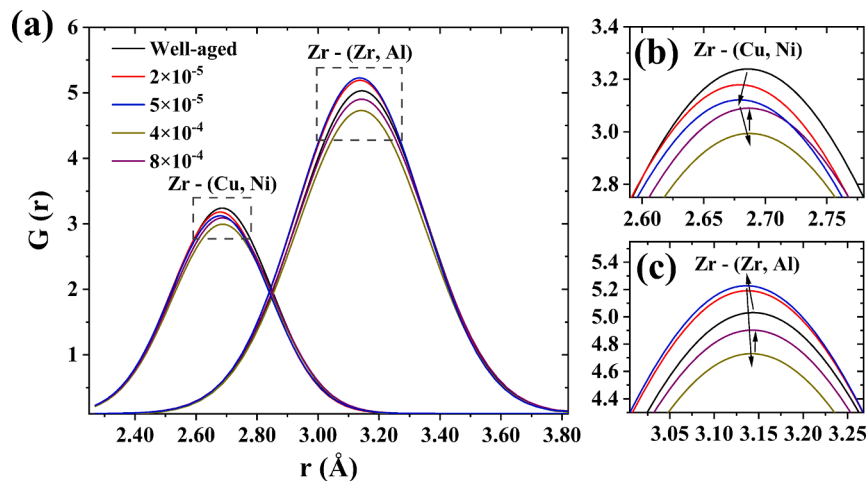
Fig. 8. Deconvolution of the first peak of $G(r)$ into two Gaussians for well-aged and deformed samples. Detailed view of (b) first peak and (c) second peak.

strain rate in Fig. 5(a).

Obviously, structural rearrangement in SRO is not sufficient to fully explain Newtonian flow rejuvenation, and it is necessary to consider the change in MRO. The enlarged second peak of the $G(r)$ is given in Fig. 7 (c), which contains the structural information of the MRO scale. It can be seen that the second peak of the $G(r)$ also splits into two sub-peaks. With Newtonian flow rejuvenation, this splitting is enhanced, which means that the structural inhomogeneity is increased and the structure is more disordered. The increase in structural disorder is also captured by the increase in $\Delta H_{eff}/\Delta H_{eff-ann}$, a statistical average quantity that contains short- and medium-range thermodynamic information. The two sub-peaks gradually polarize as strain rate increases, i.e., the first sub-peak shifts to the left and the second to the right, which reduces the mechanical stability of the structure. This demonstrates that large-scale clusters in MRO have a larger characteristic scale, which enhances the excess vibrational density of states with the enhancement of BPs. Thus, the spatial variation in the MRO explains the increase of $\Delta H_{eff}/\Delta H_{eff-ann}$ and $1/T_{BP}$ in Fig. 5. An enhancement in the height of these two sub-peaks can also be seen in Fig. 7(c), which may be ascribed to the increase in the population of Al-centered clusters mentioned in SRO. The bonding shift from Cu-centered clusters to Al-centered clusters can enlarge the number of full icosahedra and form a higher-degree medium-range structure [52]. However, the strong avoidance of Al-centered reduces the degree of interconnecting aggregation of full icosahedra, so that the medium-range order is not improved, and even more susceptible to structural disorder [53].

In non-Newtonian flow regime, the evolution of topology exhibits the remaining two stages as strain rate increases. In the first of these stages ($\dot{\varepsilon} = 4 \times 10^{-4}\ s^{-1}$), both the first and second peaks of $G(r)$ shift to lower right, reflecting the typical sign of rejuvenation that introduces free volume. It is consistent with the synchronous changes among energy level, disorder and mechanical stability reflected in Fig. 5. As the strain rate continues to increase ($\dot{\varepsilon} = 8 \times 10^{-4}\ s^{-1}$), the rejuvenation process is interrupted. The increase in the height of the PDF peaks seen in Fig. 7 is evidence of this. Such an increase in the height of the peaks is usually observed in structural relaxation, which is usually accompanied by a leftward shift in peak position [54]. This is shown in the PEL as MG trapped in a deep basin with a lower energy state. Intriguingly, in our work, we find that not only are the peak positions of $G(r)$ not shifted to the left, but the position of the second peak is significantly shifted to the right, which means a sustained expansion occurs in MRO. In typical rejuvenation, this unexpected expansion is in conflict with the reduction of atomic free volume based on thermodynamics. This conflict has been observed in many recent works and is associated with structural heterogeneity [55–57]. Chen et al. [56] systematically studied the effect of

cryogenic thermal cycling on structural rejuvenation. They suggest that rejuvenation is not only related to the number of soft regions, but also to their size. Tao et al. [58] reported similar conclusions. It can also be used to explain the conflicting results we obtained. Our results may correspond to an increase in the feature size of soft regions, but a decrease in their number. The decrease in number is manifested by the increase in the height of the PDF peaks mentioned above. The decrease of ΔH in Fig. 5 indicates that the total volume of the soft region is reduced. While $\Delta H_{eff}/\Delta H_{eff-ann}$ and $1/T_{BP}$ are more sensitive to the increase in the feature size of soft region, so they do not show a significant decrease. The rediscovery of this out of sync underscores the complexity of the PEL of MG and the importance of structural rearrangement in rejuvenation.

4. Conclusion

In this work, the relationship between rejuvenation and deformation of a well-aged Zr-based MG was systematically studied, ranging from Newtonian flow to non-Newtonian flow. Structural evolution of this MG after uniaxial homogeneous compression at different strain rates was examined in terms of their thermodynamics, vibrational dynamics, and multiscale structures. It is revealed that except for non-Newtonian flow, Newtonian flow can also rejuvenate the MG, but it is not accompanied by the increase of basin's energy level. Newtonian flow rejuvenation is attributed to multiscale structural rearrangements that reduce mechanical stability. We further find that structural rearrangement also plays a critical role when the strain rate is close to the failure strain rate. The two rejuvenation mechanisms, reduced mechanical stability and increased free volume, are decoupled again. Due to the decrease in mechanical stability induced by structural rearrangement, the critical strain rate of aging and rejuvenation of well-aged metallic glass does not correspond to that of Newtonian and non-Newtonian flow. At last, the strain rate corresponding to the upper limit of rejuvenation is not the failure strain rate.

CRediT authorship contribution statement

Y. Gao: Conceptualization, Methodology, Validation, Formal analysis, Investigation, Data curation, Writing – original draft. **G. Ding:** Methodology, Formal analysis, Resources. **C. Yang:** Investigation, Resources. **B.B. Zhang:** Investigation, Resources. **C.J. Shi:** Investigation, Resources. **L.H. Dai:** Supervision, Project administration. **M.Q. Jiang:** Conceptualization, Formal analysis, Writing – review & editing, Visualization, Supervision.

Declaration of Competing Interest

The authors declare that they have no known competing financial interests or personal relationships that could have appeared to influence the work reported in this paper.

Data availability

Data will be made available on request.

Acknowledgments

References

[1] Y.H. Sun, A. Concustell, A.L. Greer, Thermomechanical processing of metallic glasses: extending the range of the glassy state, Nat. Rev. Mater. 1 (2016) 16039.

[2] S. Kuchemann, C.Y. Liu, E.M. Dufresne, J. Shin, R. Maass, Shear banding leads to accelerated aging dynamics in a metallic glass, Phys. Rev. B 97 (2018), 014204.

[3] M. Zhang, Y.M. Wang, F.X. Li, S.Q. Jiang, M.Z. Li, L. Liu, Mechanical relaxation-to-rejuvenation transition in a Zr-based bulk metallic glass, Sci. Rep.-Uk 7 (2017) 625.

[4] Y. Tong, W. Dmowski, H. Bei, Y. Yokoyama, T. Egami, Mechanical rejuvenation in bulk metallic glass induced by thermo-mechanical creep, Acta Mater. 148 (2018) 384–390.

[5] M.Q. Jiang, Y. Gao, Structural rejuvenation of metallic glasses and its effect on mechanical behaviors, Acta Metall. Sin. 57 (2021) 425–438.

[6] M.Q. Jiang, L. Dai, Mechanics of amorphous solids, Chinese Sci. Bull. 67 (2022) 2578–2593.

[7] H. Kato, Y. Kawamura, A. Inoue, H.S. Chen, Newtonian to non-Newtonian master flow curves of a bulk glass alloy Pd40Ni10Cu30P20, Appl. Phys. Lett. 73 (1998) 3665–3667.

[8] J. Lu, G. Ravichandran, W.L. Johnson, Deformation behavior of the Zr41.2Ti13.8Cu12.5Ni10Be22.5 bulk metallic glass over a wide range of strain-rates and temperatures, Acta Mater. 51 (2003) 3429–3443.

[9] M. Bletry, P. Guyot, J.J. Blandin, J.L. Soubeyroux, Free volume model: high-temperature deformation of a Zr-based bulk metallic glass, Acta Mater. 54 (2006) 1257–1263.

[10] L.T. Zhang, Y.J. Duan, D. Crespo, E. Pineda, T. Wada, H. Kato, J.M. Pelletier, J.C. Qiao, Identifying the high entropy characteristic in La-based metallic glasses, Appl. Phys. Lett. 119 (2021) 051905.

[11] L. Li, N. Wang, F. Yan, Transient response in metallic glass deformation: a study based on shear transformation zone dynamics simulations, Scr. Mater. 80 (2014) 25–28.

[12] M.Q. Jiang, G. Wilde, L.H. Dai, Origin of stress overshoot in amorphous solids, Mech. Mater. 81 (2015) 72–83.

[13] G. Ding, F. Jiang, L.H. Dai, M.Q. Jiang, Effective energy density of glass rejuvenation, Acta Mech. Solida Sin. (2022) 746–754.

[14] H. Kato, A. Inoue, H.S. Chen, Heating and structural disordering effects of the nonlinear viscous flow in a Zr55Al10Ni5Cu30 bulk metallic glass, Appl. Phys. Lett. 83 (2003) 5401–5403.

[15] Z. Fan, J. Ding, E. Ma, Machine learning bridges local static structure with multiple properties in metallic glasses, Mater. Today 40 (2020) 48–62.

[16] Y. Gao, C. Yang, G. Ding, L.-H. Dai, M.-Q. Jiang, Structural rejuvenation of a well-aged metallic glass, Fundam. Res. (2022) https://doi.org/10.1016/j.fmre.2022.12.004.

[17] H.B. Zhou, R. Hubek, M. Peterlechner, G. Wilde, Two-stage rejuvenation and the correlation between rejuvenation behavior and the boson heat capacity peak of a bulk metallic glass, Acta Mater. 179 (2019) 308–316.

[18] L.T. Zhang, Y.J. Wang, Y. Yang, J.C. Qiao, Aging and rejuvenation during high-temperature deformation in a metallic glass, Sci. China. Phys. Mech. 65 (2022), 106111.

[19] H. Jin, J. Wen, K. Lu, Shear stress induced reduction of glass transition temperature in a bulk metallic glass, Acta Mater 53 (2005) 3013–3020.

[20] X. Yuan, D. Sopu, F. Spieckermann, K.K. Song, S.V. Ketov, K.G. Prashanth, J. Eckert, Maximizing the degree of rejuvenation in metallic glasses, Scr. Mater. 212 (2022), 114575.

[21] F. Sette, M.H. Krisch, C. Masciovecchio, G. Ruocco, G. Monaco, Dynamics of glasses and glass-forming liquids studied by inelastic X-ray scattering, Science 280 (1998) 1550–1555.

[22] G. Ding, C. Li, A. Zaccone, W.H. Wang, H.C. Lei, F. Jiang, Z. Ling, M.Q. Jiang, Ultrafast extreme rejuvenation of metallic glasses by shock compression, Sci. Adv. 5 (2019) eaaw6249.

[23] A.P. Hammersley, S.O. Svensson, M. Hanfland, A.N. Fitch, D. Hausermann, Two-dimensional detector software: from real detector to idealised image or two-theta scan, High Pressure Res. 14 (1996) 235–248.

[24] X. Qiu, J.W. Thompson, S.J.L. Billinge, PDFgetX2: a GUI-driven program to obtain the pair distribution function from X-ray powder diffraction data, J. Appl. Crystallogr. 37 (2004) 678.

[25] M. Zhang, L.H. Dai, L. Liu, Mechanical annealing in the flow of supercooled metallic liquid, J. Appl. Phys. 116 (2014), 053522.

[26] C.A. Angell, Relaxation in liquids, polymers and plastic crystals - strong fragile patterns and problems, J. Non-Cryst. Solids 131 (1991) 13–31.

[27] J. Saida, S. Ishihara, H. Kato, A. Inoue, H.S. Chen, Suppression of quasicrystallization by nonlinear viscous flow in Zr-Al-Ni-Cu-Pd glassy alloys, Appl. Phys. Lett. 80 (2002) 4708–4710.

[28] P. Cao, M.P. Short, S. Yip, Potential energy landscape activations governing plastic flows in glass rheology, P. Natl. Acad. Sci. U.S.A. 116 (2019) 18790–18797.

[29] Y.T. Cheng, Q. Hao, J.M. Pelletier, E. Pineda, J.C. Qiao, Modelling and physical analysis of the high-temperature rheological behavior of a metallic glass, Int. J. Plast. 146 (2021) 103107.

[30] J.C. Qiao, J.M. Pelletier, Dynamic mechanical relaxation in bulk metallic glasses: a review, J. Mater. Sci. Technol. 30 (2014) 523–545.

[31] Y. Tong, T. Iwashita, W. Dmowski, H. Bei, Y. Yokoyama, T. Egami, Structural rejuvenation in bulk metallic glasses, Acta Mater. 86 (2015) 240–246.

[32] Y.H. Liu, G. Wang, R.J. Wang, D.Q. Zhao, M.X. Pan, W.H. Wang, Super plastic bulk metallic glasses at room temperature, Science 315 (2007) 1385–1388.

[33] H.B. Zhou, V. Khonik, G. Wilde, On the shear modulus and thermal effects during structural relaxation of a model metallic glass: correlation and thermal decoupling, J. Mater. Sci. Technol. 103 (2022) 144–151.

[34] M.Q. Jiang, M. Peterlechner, Y.J. Wang, W.H. Wang, F. Jiang, L.H. Dai, G. Wilde, Universal structural softening in metallic glasses indicated by boson heat capacity peak, Appl. Phys. Lett. 111 (2017), 261901.

[35] M. Bletry, P. Guyot, Y. Brechet, J.J. Blandin, J.L. Soubeyroux, Homogeneous deformation of Zr-Ti-Al-Cu-Ni bulk metallic glasses, Intermetallics 12 (2004) 1051–1055.

[36] J. Yang, Y.J. Wang, E. Ma, A. Zaccone, L.H. Dai, M.Q. Jiang, Structural parameter of orientational order to predict the boson vibrational anomaly in glasses, Phys. Rev. Lett. 122 (2019), 015501.

[37] J. Ding, S. Patinet, M.L. Falk, Y.Q. Cheng, E. Ma, Soft spots and their structural signature in a metallic glass, P. Natl. Acad. Sci. U.S.A. 111 (2014) 14052–14056.

[38] Z.Y. Yang, Y.J. Wang, A. Zaccone, Correlation between vibrational anomalies and emergent anharmonicity of the local potential energy landscape in metallic glasses, Phys. Rev. B 105 (2022), 014204.

[39] J. Pan, Y.P. Ivanov, W.H. Zhou, Y. Li, A.L. Greer, Strain-hardening and suppression of shear-banding in rejuvenated bulk metallic glass, Nature 578 (2020) 559–562.

[40] G. Ding, F. Jiang, X. Song, L.H. Dai, M.Q. Jiang, Unravelling the threshold stress of structural rejuvenation of metallic glasses via thermo-mechanical creep, Sci. China Phys. Mech. 65 (2022), 264613.

[41] J. Ding, Y.Q. Cheng, H. Sheng, M. Asta, R.O. Ritchie, E. Ma, Universal structural parameter to quantitatively predict metallic glass properties, Nat. Commun. 7 (2016) 13733.

[42] X.Y. Gong, X.D. Wang, P. Zhang, X.Z. Cao, Q.P. Cao, D.X. Zhang, J.Z. Jiang, Structural rejuvenation in a Zr-based bulk metallic glass via electropulsing treatment, Appl. Phys. Lett. 119 (2021), 043901.

[43] L. Cervinka, Modeling of medium-range order in metallic glasses - calculation of X-ray-scattering in a Ti61Cu16Ni23 glass, J. Non-Cryst. Solids 156 (1993) 94–97.

[44] S. Scudino, M. Stoica, I. Kaban, K.G. Prashanth, G.B.M. Vaughan, J. Eckert, Length scale-dependent structural relaxation in Zr57.5Ti7.5Nb5Cu12.5Ni10Al7.5 metallic glass, J. Alloys Compd. 639 (2015) 465–469.

[45] X. Tong, G. Wang, Z.H. Stachurski, J. Bednarcik, N. Mattern, Q.J. Zhai, J. Eckert, Structural evolution and strength change of a metallic glass at different temperatures, Sci. Rep.-Uk 6 (2016) 30876.

[46] T. Egami and S.J.L. Billinge, Underneath the Bragg Peaks Structural Analysis of Complex Materials Preface, Underneath the Bragg Peaks: Structural Analysis of Complex Materials, 1st Edition Vol. 7 (2003) VII-X.

[47] M. Stoica, J. Das, J. Bednarcik, H. Franz, N. Mattern, W.H. Wang, J. Eckert, Strain distribution in Zr64.13Cu15.75Ni10.12Al10 bulk metallic glass investigated by in situ tensile tests under synchrotron radiation, J. Appl. Phys. 104 (2008), 013522.

[48] T. Iwashita, T. Egami, Atomic mechanism of flow in simple liquids under shear, Phys. Rev. Lett. 108 (2012), 196001.

[49] Y.H. Liu, T. Fujita, D.P.B. Aji, M. Matsuura, M.W. Chen, Structural origins of Johari-Goldstein relaxation in a metallic glass, Nat. Commun. 5 (2014) 3238.

[50] M. Samavatian, R. Gholamipour, A.A. Amadeh, S. Mirdamadi, Extra rejuvenation of Zr55Cu30Al10Ni5 bulk metallic glass using elastostatic loading and cryothermal treatment interaction, J. Non-Cryst. Solids 506 (2019) 39–45.

[51] J.F. Zhao, A. Inoue, C.T. Liu, P.K. Liaw, X.P. Shen, S.Y. Pan, G. Chen, C. Fan, Structural evolution and energy landscape of the clusters in Zr55Cu35Al10 metallic liquid and glass, Scr. Mater. 117 (2016) 64–67.

[52] Y.Q. Cheng, E. Ma, H.W. Sheng, Atomic level structure in multicomponent bulk metallic glass, Phys. Rev. Lett. 102 (2009) 245501.

[53] H.K. Kim, M. Lee, K.R. Lee, J.C. Lee, How can a minor element added to a binary amorphous alloy simultaneously improve the plasticity and glass-forming ability? Acta Mater. 61 (2013) 6597–6608.

[54] W. Dmowski, C. Fan, M.L. Morrison, P.K. Liaw, T. Egami, Structural changes in bulk metallic glass after annealing below the glass-transition temperature, Mat. Sci. Eng. A-Struct. 471 (2007) 125–129.

[55] X.L. Bian, G. Wang, J. Yi, Y.D. Jia, J. Bednarcik, Q.J. Zhai, I. Kaban, B. Sarac, M. Muhlbacher, F. Spieckermann, J. Keckes, J. Eckert, Atomic origin for

rejuvenation of a Zr-based metallic glass at cryogenic temperature, J. Alloys Compd. 718 (2017) 254–259.

[56] H. Chen, Y. Hai, R. Li, K. Sun, J. Xu, Y.G. Xia, G. Wang, W. Yin, Defects controlled rejuvenation in the Zr47.5Cu47.5Al5 metallic glass, J. Alloys Compd. 927 (2022), 166876.

[57] H.W. Luan, X. Zhang, H.Y. Ding, F. Zhang, J.H. Luan, Z.B. Jiao, Y.C. Yang, H.T. Bu, R.B. Wang, J.L. Gu, C.L. Shao, Q. Yu, Y. Shao, Q.S. Zeng, N. Chen, C.T. Liu, K.

F. Yao, High-entropy induced a glass-to-glass transition in a metallic glass, Nat. Commun. 13 (2022) 2183.

[58] K. Tao, J.C. Qiao, Q.F. He, K.K. Song, Y. Yang, Revealing the structural heterogeneity of metallic glass: mechanical and nanoindentation, Int. J. Mech. Sci. 201 (2021), 106469.